



Observation of charge conduction mechanism of manganese ferrite—poly (vinyl alcohol) nanocomposite film above room temperature

Monalisa Halder¹, Shubhadip Atta¹, Ranjita Sinha², and Ajit Kumar Meikap^{1,*}

¹Department of Physics, National Institute of Technology, Durgapur 713209, India

²Department of BS&HU(Physics), Asansol Engineering College, Asansol 713305, India

Received: 25 April 2022

Accepted: 12 August 2022

Published online:
26 August 2022

© The Author(s), under exclusive licence to Springer Science+Business Media, LLC, part of Springer Nature 2022

ABSTRACT

This article reports the investigation on charge transport mechanism in manganese ferrite loaded polyvinyl alcohol (MFO-PVA) nanocomposite film. The basic structure of pure PVA film and the nanocomposite film (MFO-PVA) is studied using the X-ray diffraction technique. With the loading of MFO NPs in the PVA matrix, the conductivity of the composite enhances. The dielectric constant of MFO-PVA film is higher than that of pristine PVA one. The nanocomposite film also exhibits low tangent loss. The current voltage characteristics can be explained using the thermionic emission (TE) and Schottky emission (SE) models considering back-to-back Schottky diode formation. Oxygen-related defect states exist in the polymeric system, which exhibits trapping of the charge carriers.

1 Introduction

Polymer nanocomposites have drawn significant attention from an academic and technological perspective because of their unique physical properties and potential applications in nanoelectronics, electromagnetic and biomedical devices [1]. This is a very familiar process for enhancing the mechanical, optical, thermal, electrical, and magnetic characteristics of the standard polymeric system by adding a little amount of nanofiller into it without much change in the processing [2]. On the other hand, microwave absorbing materials play a significant role in

electromagnetic pollution, electromagnetic interference, shielding, etc. [3]. Researches are going on about spinel ferrites as the most frequent absorbing material. Manganese ferrite (MFO) is a common spinel ferrite material for magnetic recording and microwave applications [3]. MFO has high magnetization ability because of its sizeable magnetic spin, large permeability, high resistivity, and low dielectric loss [4]. MFO loaded polyvinyl alcohol nanocomposite system can be potentially applicable in various fields. In the present work, MFO nanoparticles are dispersed in a PVA matrix. Among several polymers, polyvinyl alcohol (PVA) is a broadly utilized as non-

Address correspondence to E-mail: meikapnitd@yahoo.com

toxic and flexible matrix element as it has good electrical properties, excellent tensile strength, and functional charge storage capacity [5]. The inclusion of nanosized magneto-electric materials can significantly affect the dielectric/magneto-dielectric response, charge conduction mechanism in the polymeric system. Hosseini et al. [3] reported various properties of polyaniline and manganese ferrite nanocomposites. Huang et al. [6] synthesized magnetic epoxy nanocomposites with superparamagnetic MFO nanoparticles. Shafiu et al. [7] worked on the facile synthesis of PVA-MnFe₂O₄ nanocomposite. The composite has a superparamagnetic character at room temperature and a ferromagnetic character at low temperature. Rezaei et al. [8] the role of PVA surfactant on magnetic properties of MFO nanoparticles synthesized by sol-gel hydrothermal method. Nasar et al. [9] reported the successful synthesis and characterisation of magnesium ferrite/PVA nanocomposites. Alhusaiki-Alghamdi et al. [10] reported the effect of addition of MFO nanoparticles on polyvinyl alcohol/polyethylene glycol blend for magnetoelectronics and optoelectronics applications. Salah et al. [11] reported the fabrication and characterization of nanocomposite flexible membranes of PVA and Fe₃O₄. Sahanakumari et al. [12] effectively modified the microstructural, optical and electrical properties of PVA by zinc ferrite nano fillers.

The present article reports the charge conduction process of pure PVA and manganese ferrite loaded PVA (MFO-PVA) film samples using the impedance spectroscopy and current-voltage relation. Here DC conductivity, frequency-dependent dielectric loss, and complex impedance spectroscopy of the samples are studied. Considering Schottky diode formation, variation of current with voltage application is also studied using different appropriate models.

2 Experimental details

All analytically pure precursor materials are purchased from Sigma-Aldrich and are used without any further purification. MnFe₂O₄ (MFO) nanoparticles were synthesized using chloride precursors. Polyvinyl alcohol (PVA) film was prepared by the drop-casting method. Previously synthesized MnFe₂O₄ (MFO) nanoparticles of 1wt% are mixed in polyvinyl alcohol (PVA) solution. By the drop-casting method, the nanocomposite film (MFO-PVA) is achieved,

followed by natural drying. The detailed procedure has been discussed in our previously published work in detail [13]. The digital images of the films are displayed in Fig. 1.

XRD data of the samples (pure PVA & MFO-PVA) are taken by X'pert Pro multi-purpose diffractometer (PANALYTICAL) using Cu K α radiation from in 2 θ range from 20° to 80°. Here the charge transport mechanism of the film is observed intricately above room temperature. A parallel plate capacitive configuration is adopted to study the electrical properties of the samples. A small square shaped section of each film sample of average breadth of 0.090 ± 0.001 mm and area of 1×1 cm² was taken for the observation. Metallic electrodes (Silver paste, Acheson Colloiden B. V Holland) were connected to the opposite faces of the square-shaped sample material. DC electrical measurement was done using Keithley 6514 electrometer with two probe method. Temperature dependence of dielectric response and impedance spectroscopy were studied using a furnace fitted with 8502 Eurotherm temperature controller cryostat in temperature range 315–410 K. The AC conductivity and dielectric properties are studied in the frequency range 20 Hz–2 MHz with an Agilent E 4980A precision LCR meter. The current-voltage properties of the film samples are recorded using Keithley 2450 source measure unit (SMU) equipped with KickStart software.

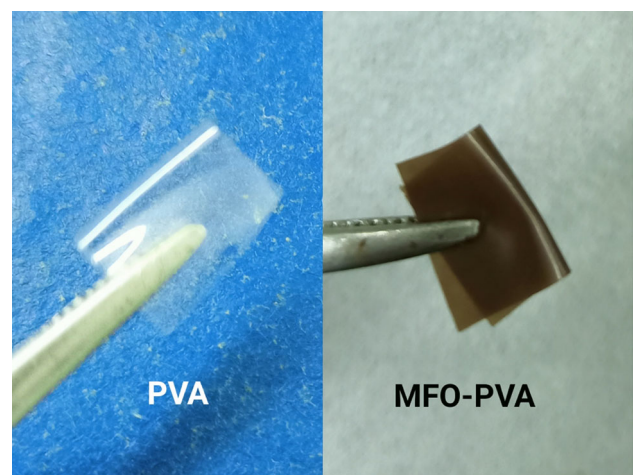


Fig. 1 Digital images of PVA and MFO-PVA films.

3 Results and discussions

3.1 X-Ray diffraction study

Figure 2 illustrates the room temperature XRD patterns of pure PVA and MFO-PVA films, respectively. Pure PVA shows diffraction peaks at $2\theta = 20^\circ$, $2\theta = 21.3^\circ$ and $2\theta = 41.3^\circ$, which correspond to the semi-crystalline phase of PVA polymer. In MFO-PVA film, diffraction peaks correspond to the MFO inserted in PVA are observed clearly. The sharp peaks of MFO NPs go well with the standard recorded reference data (JCPDS Card No: 88–1965) and confirm MFO nanoparticles' inclusion in the PVA polymeric matrix. Determination of crystallite size (volume weighed domain size in the direction parallel to the diffraction vector) D is calculated using the Debye Scherrer formula [14],

$$D = \frac{K\lambda}{\beta \cos \theta} \tag{1}$$

where K is Scherrer constant, λ is the X-ray wavelength, 2θ is the Bragg angle for reflection, β is the full width at half maximum intensity of the peak (in Rad). Crystallite size and lattice strain of pure PVA and MFO-PVA films can be calculated using Williamson–Hall (W–H) method, where both strain-induced broadening and size broadening have been considered and given as [15]

$$\beta \cos \theta = \frac{K\lambda}{D} + 4\epsilon \sin \theta \tag{2}$$

where the term $K\lambda/D$ comes from the Scherrer equation [16]. The W–H method is applied for the film samples to obtain the values of crystallite size and strain from the y-intercept and the slope of the best fitted straight line, respectively (Table 1). Figure 3 displays the Williamson–Hall plot of the film samples. The negative value of strain indicates the lattice compression/shrinkage effect.

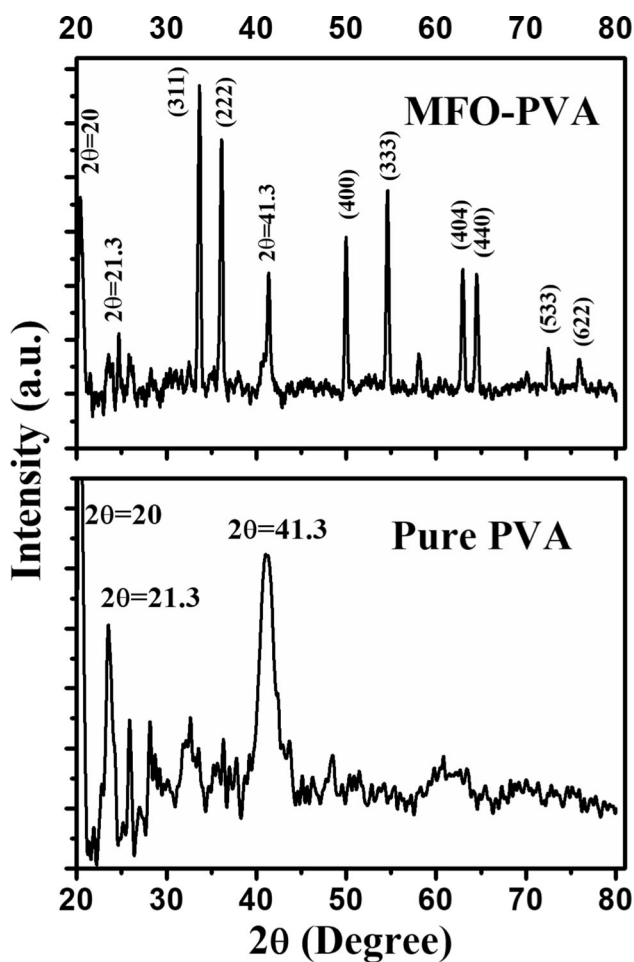


Fig. 2 X-ray diffraction pattern of Pure PVA and MFO-PVA films

3.2 DC conductivity study

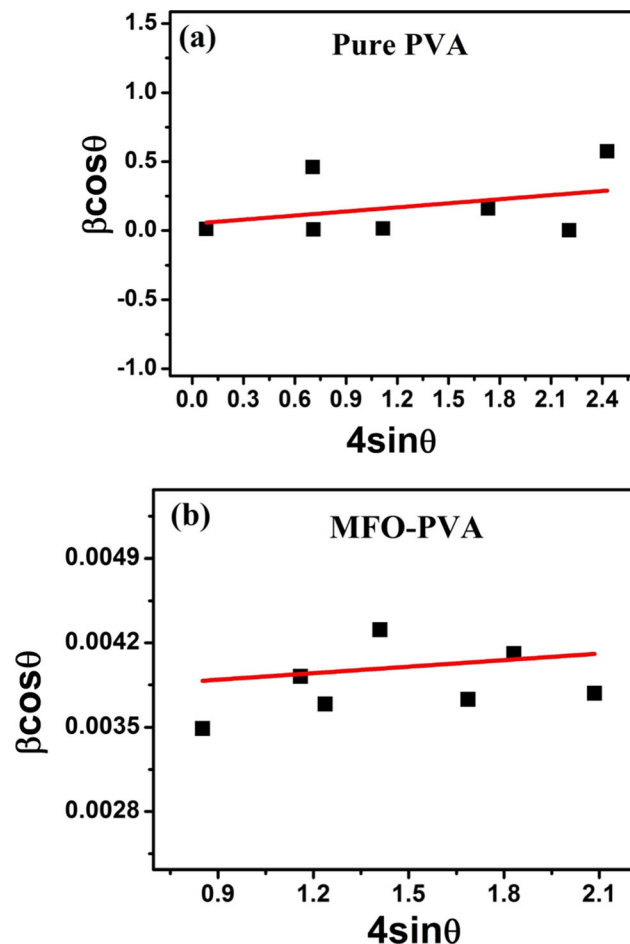
Temperature-dependent DC conductivity is studied in the temperature range $300\text{ K} \leq T \leq 410\text{ K}$ to get an idea about the films' electrical conduction mechanism. The conductivity rises with the increasing temperature. So, both the samples exhibit negative temperature coefficient of resistance (NTCR) behavior. Arrhenius formalism of conductivity can be applied to get the values of the films' activation energies [17].

$$\sigma_{dc}(T) = \sigma_0 \exp \left[-\left(\frac{E_A}{k_B T} \right) \right] \tag{3}$$

where σ_0 is a constant, E_A is the activation energy, and k_B is Boltzmann's constant. From the Eq. (3), the values of activation energy (E_A) in high and low temperatures can be determined from the slope of $\ln \sigma_{dc}$ vs. $1000/T$ plot (Fig. 4). The extracted values of activation energies of the films are given in Table 2. With the inclusion of MFO nanofiller in the polymeric system, DC conductivity increases. The activation energy is reduced when temperature increases. When MFO is loaded in the PVA matrix, then also the value of activation energy gets reduced indicating increased hopping of the charge carrier concentration between the neighbouring lattice sites.

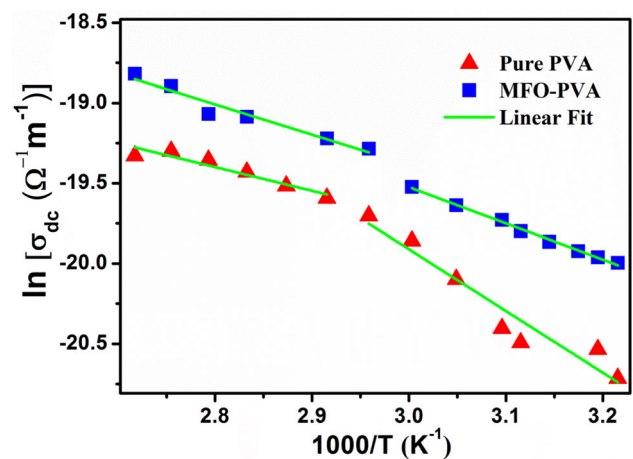
Table 1. Derived parameters from XRD analysis and Williamson-Hall plot

Samples	Crystallite size from Debye–Scherrer Equation (nm)	Crystallite size from hall plot (nm)	Strain (10^{-3})
PVA	12.7	8.4	−1.52
MFO-PVA	30.9	26.7	−6.15

**Fig. 3** a Williamson-Hall plot of pure PVA sample, b Williamson-Hall plot of MFO-PVA film sample.

3.3 Dielectric response and dielectric loss study

The temperature variation of the dielectric constant of the film samples at different frequencies is shown in Fig. 5a. In both the samples, at higher temperature region as well as in lower frequencies, the temperature dispersion of dielectric response is more notable. With the rise in temperature, the dielectric curves get steeper. A considerable variation of dielectric constant with temperature has been perceived in the lower frequency regime than the high frequencies. In

**Fig. 4** Temperature variation of DC conductivity of PVA and MFO-PVA films.**Table 2.** Derived electrical parameters of the film samples from DC conductivity and current–voltage characteristics study

Parameters		PVA	MFO-PVA
σ_0 (S/m)	High temperature	1.1×10^{-6}	2.4×10^{-7}
	Low temperature	2.9×10^{-6}	2.2×10^{-4}
E_A (eV)	High temperature	0.16	0.12
	Low temperature	0.28	0.22
ϕ_B (meV)		14	11
A^* ($A \text{ cm}^{-2} \text{ K}^{-2}$)		6.59×10^{-5}	2.33×10^{-5}
I_s (A)(K)	316	2.2×10^{-7}	1.9×10^{-7}
	333	8.1×10^{-7}	6.9×10^{-7}
	353	1.2×10^{-6}	8.6×10^{-7}
	388	1.9×10^{-5}	2.1×10^{-5}
ϵ_r (K)	403	1.3×10^{-5}	1.6×10^{-5}
	316	1.7×10^{-3}	2.5×10^{-3}
	333	8.7×10^{-4}	1.1×10^{-3}
	353	8.9×10^{-4}	9.4×10^{-4}
	388	1.2×10^{-5}	1.5×10^{-5}

a lower frequency regime, electronic polarizability (electrons shifting within molecules) and orientational polarizability (dipolar molecules rotating or flipping, or ions changing places) contributes to the relative permittivity. But in higher frequencies, the sample's net polarisation drops as each polarisation

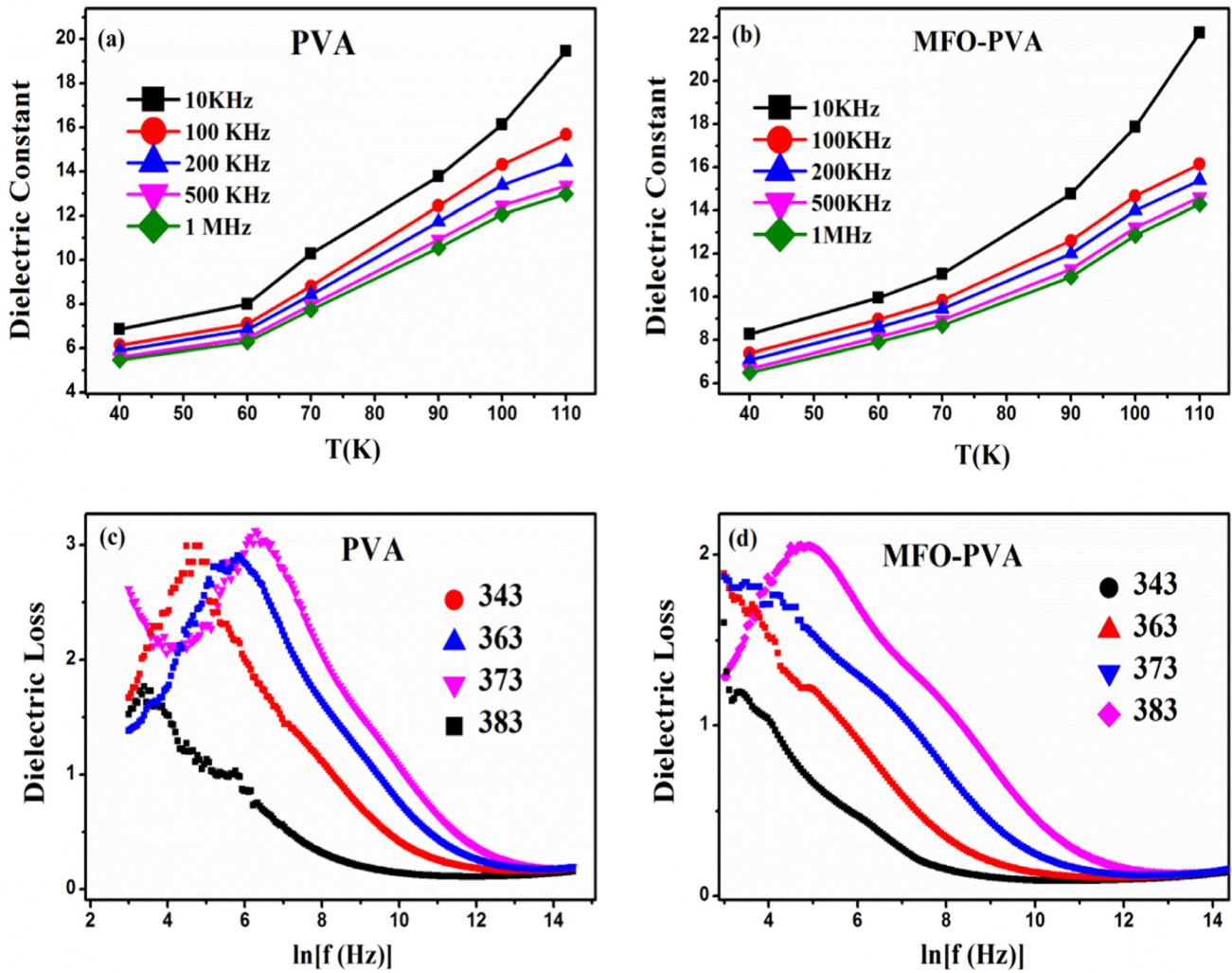


Fig. 5 a–b The temperature variation of the dielectric constant of PVA and MFO-PVA films at different frequencies respectively, c–d frequency variation of dielectric loss of PVA and MFO-PVA films, respectively.

mechanism ceases to contribute, and hence its dielectric constant drops [18]. The dielectric material becomes polarized in an applied electric field. For the material to get polarized, some time span (relaxation time) is needed to orient the dipoles according to the direction of applied field. So if the direction of applied field changes rapidly, the dipoles inside the material may not be able to reorient themselves at this frequency, and hence at higher frequencies, the dielectric constant drops down [19]. In lower temperatures, electric dipole movement stops easily, but in higher temperature regions, space charge polarization/electrode polarization increases the dielectric constant value [20].

The dielectric constant is enhanced when MFO nanofiller is included in the PVA matrix. Figure 5b

shows the frequency variation of loss tangent [$\tan\delta$] in the frequency range 20 Hz–2 MHz for the film samples at different temperatures. A notable relaxation peak is present in the dielectric loss curve of the nanocomposite sample. The relaxation peak exists because of the increase in mobility in the polymer chain. Usually, the highest temperature peak in $\tan\delta$ curve is taken to indicate the glass transition temperature (peak temperature). The peak shifts to the higher frequency region with the increase in temperature. Relaxation peak intensity tends to lower with the decrement of temperature. The peak intensity also decreases in MFO-PVA nanocomposite films than that of pristine PVA film. This result is desirable for the use of the nanocomposite in potential applications.

3.4 Impedance spectroscopy study

The functional dielectric response of a heterogeneous system is better understood by complex impedance spectroscopy more often. Complex impedance spectroscopy (CIS) technique is used to characterise materials by studying the electrical and dielectric properties of the material. It is used to separate the contributions of grains and grain boundaries to the transport properties of materials [21]. Maxwell–Wagner capacitor model is taken here to understand the complex impedance of the sample i.e.

$$Z = \frac{1}{i2\pi f C_0 \varepsilon(f)} = Z'(f) - iZ''(f) \quad (4)$$

where $Z'(f)$ and $Z''(f)$ are the real and imaginary parts of complex impedance, respectively, C_0 is the free space capacitance. Figure 6a, b exhibit the frequency dependence of the real part and imaginary part of impedance spectra of MFO-PVA nanocomposite film samples at different measuring temperatures, respectively. At low frequencies, the free dipoles align themselves along the field present in the composite system. But in higher frequencies, the dipoles are not able to move so fast within short time period. When temperature is reduced, both the frequency dependent curves of the real part and the imaginary part of impedance spectra become more responsive. We can conclude that the space charge polarization and the mobility in the film sample get enhanced with temperature. Figure 7 shows the Nyquist plot (imaginary impedance [$Z''(f)$] vs. real impedance [$Z'(f)$]) of the nanocomposite films at different temperatures. The complex impedance plots have semicircular arc in the higher frequency region. The semicircular arc has a tendency to form two depressed semicircular arcs indicating the contribution of both grain and grain boundary to the electric conductivity. Here, the arc's center is depressed and lies below the real impedance axis showing non-Debye type behavior [22]. The diameter of the semicircle decreases as temperature increases. As a result, the sample's bulk resistance decreases, showing NTCR (negative temperature coefficient of resistance) behavior like that of a semiconductor.

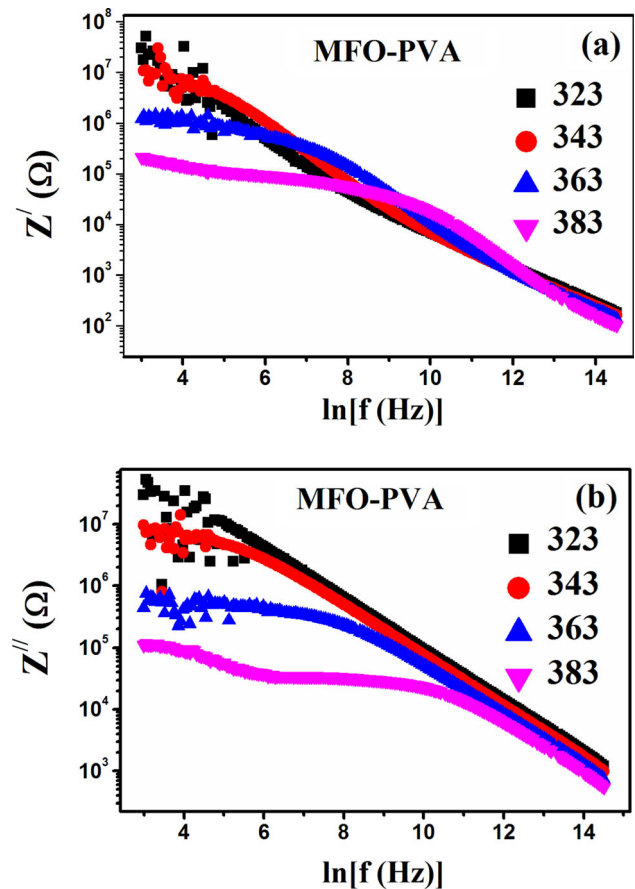


Fig. 6 a Real part of impedance (Z') spectra of the MFO-PVA nanocomposite sample, b Imaginary part of impedance (Z'') spectra of the sample.

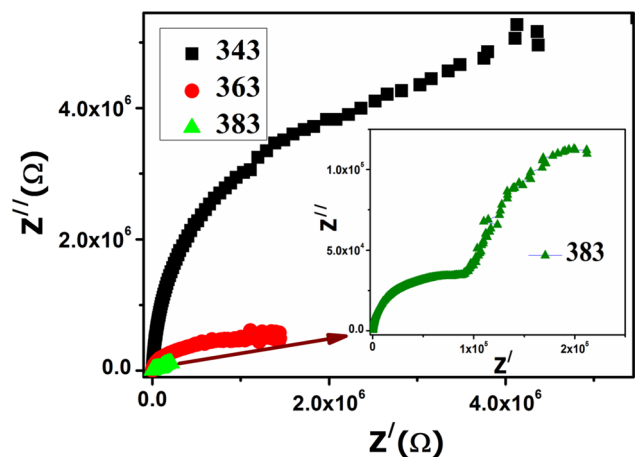


Fig. 7 Nyquist plot of the MFO-PVA nanocomposite film at different temperatures.

3.5 Non-linear current–voltage characteristics study

The electrical conductivity of a semiconducting material depends on the concentration of charge carrier and their mobility, which depends on both the concentration of impurities/doping and the temperature. By forming two metal–semiconductor junctions (Ag electrodes have been connected on both sides of the film sample), Schottky barrier diode (SBD) is constructed. The non-linear temperature-dependent I–V characteristics of the film samples (pure PVA and MFO-PVA) are shown in Fig. 8a, b at different temperatures. Current is increasing with the increase in temperature. To further discuss the samples’ conduction mechanism, the current–voltage (I–V) characteristics are analyzed using the well-known

thermionic emission (TE) theory. For an SBD, I–V relation can be stated using Richardson equation [23],
$$I = I_S[\exp\{q(V - IR)/nkT\} - 1]$$
 (5)

where I is the forward diode current and reverse saturation current I_S can be explained as

$$I_S = AA * T^2 \exp\left(-\frac{q\phi_b}{kT}\right)$$
 (6)

where q is the electric charge, A is the area of the sample, A^* is modified Richardson constant, T is the temperature expressed in Kelvin scale, R is the resistance, n is the ideality factor, ϕ_B is the effective barrier height, and k is Boltzmann’s constant. The extracted values of the ideality factor are plotted against temperature in Fig. 9b. A significant value of the ideality factor arises because of the recombination current and high leakage current in the samples. Ideality factor decreases with temperature. Large value of ideality factor arises by interfacial layer and surface states of the sample. The tunneling mechanism is dominant for charge conduction. Linear variation of Richardson plot (Fig. 9b) suggests the existence of ideal heterojunction case [24]. From the slope and the intercept of the linear fit of the Richardson plot, effective barrier height (ϕ_B) and modified Richardson constant (A^*) can be determined, respectively (Table 2). The effective barrier height gets lowered when MFO nanofiller is included in the polymeric matrix. The better ideality factor of MFO-PVA nanocomposite arises may be due to the enhancement of the charge transport across the interface. But in both the film samples, the ideality factor is larger than one.

To further discuss the conduction mechanism within the film samples, the current–voltage (I–V) characteristics are analyzed using well known Schottky emission (SE) model. Generally, the charge transport phenomenon in a metal/semiconducting sample/metal parallel type capacitive system can be categorised into two basic groups. One group considers the electrode limited conduction mechanism, i.e., the nature of injection of charge carriers from the metal electrode to semiconductor. Another is related to the semiconducting material’s bulk properties, where transport of charge carriers takes place through semiconductors [25]. Schottky emission (SE) and Fowler–Nordheim (FN) tunneling is included into the first group, whereas space charge limited conduction (SCLC), Poole–Frenkel (PF) emission and

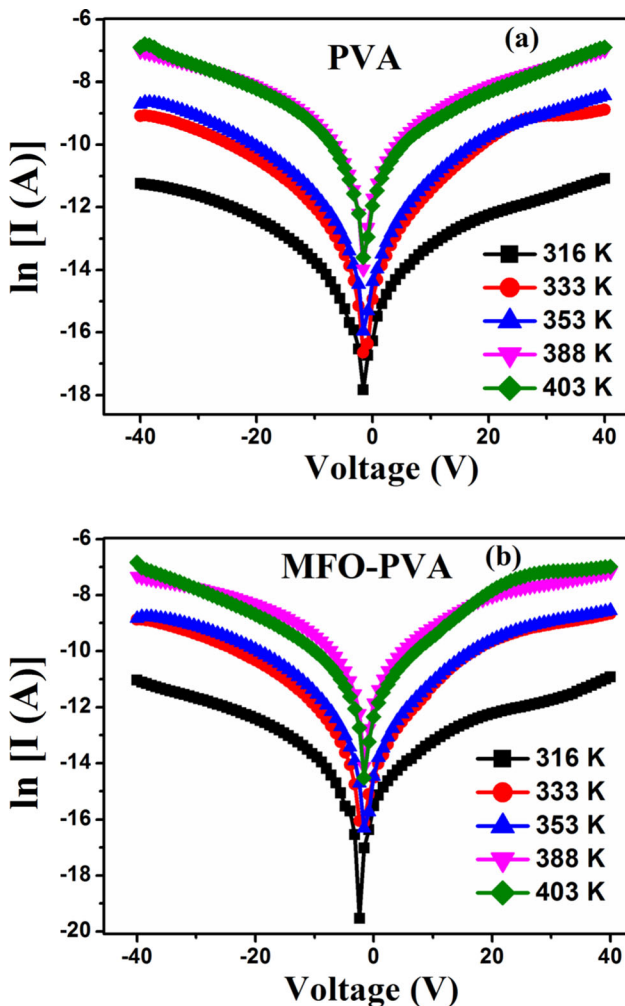


Fig. 8 a–b ln I vs. V curves of PVA and MFO-PVA films respectively at different temperatures.

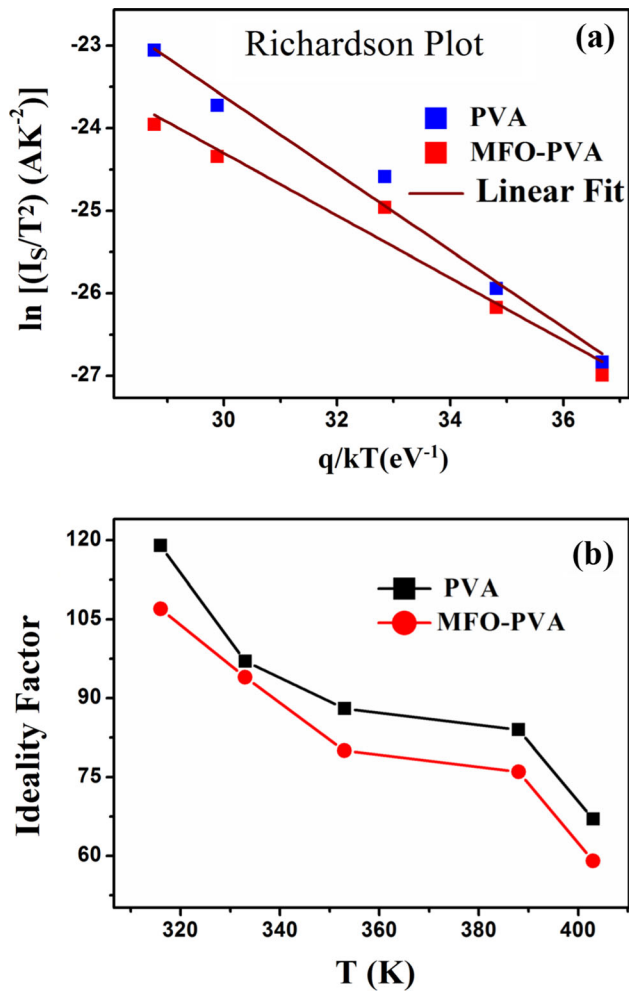


Fig. 9 **a** Richardson plot of $\ln(I_s/T^2)$ vs. q/kT of the film samples at different temperatures, **b** temperature variation of ideality factor of the film samples.

Ohmic conduction mechanism belong to the second group [20]. In the present work, the experimental data is simulated using the Schottky emission (SE) model. According to this model, the current density is generally stated as,

$$J_{SE} = A^* T^2 \exp \left[-\frac{q\phi_B - \sqrt{q^3 E / 4\pi\epsilon_0\epsilon_r}}{k_B T} \right] \quad (7)$$

where A^* is the effective Richardson's constant, ϕ_B is the Schottky barrier height at 0 applied field, q is the electronic charge, ϵ_0 is the dielectric constant in vacuum, ϵ_r is the optical dielectric constant, and k_B is Boltzmann's constant. According to SE model, free charges transit from the metal plate to the film sample in the presence of trap states/defect states. By applying an external electric field, electrons get

excited and get out from the trap states. This kind of charge conduction phenomenon is relevant and suitable for both forward and reverse external field applications [26]. Figure 10a, b show $\ln J$ vs. $E^{1/2}$ plots of the film samples at different temperatures. The values ϵ_r are listed in Table 2. For both the samples, the optical dielectric constant value decreases with the increase in temperature since the thermal agitation opposes the alignment of electric dipoles under the action of the applied electric field.

4 Conclusion

In this work, we report an observation on the charge conduction mechanism in the MFO-PVA nanocomposite film system above room temperature. MFO

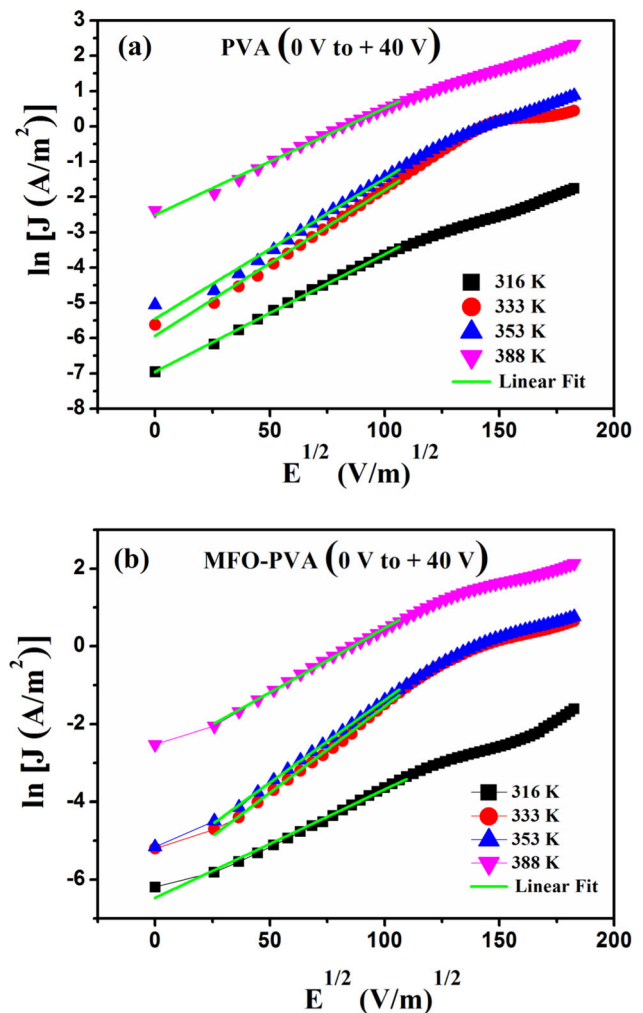


Fig. 10 **a–b** $\ln J$ vs. $E^{1/2}$ plots using SE model PVA and MFO-PVA films respectively at different temperatures.

loaded PVA film is synthesized by the simple drop-casting method. The variation of DC conductivity is measured as a function of temperature ranging from 300 K to 410 K. Applying Arrhenius formalism, activation energies are calculated. The presence of multiple activation energies suggests hopping type current conduction mechanisms at different temperature regions. The dielectric property and current–voltage (I–V) characteristics of the films are studied to elucidate the practical applications. Frequency dependence of real and imaginary parts of dielectric constant with different temperatures for MFO-PVA nanocomposite films are studied in the frequency range 20 Hz–2 MHz. Complex impedance plots of the film samples clearly presents both the grain and grain boundary contributions. Current–voltage characteristics of the film samples show nonlinearity conceptualizing the Schottky diode model. Due to the generation of recombination current and high leakage current, a significant value of ideality factor arises in the film sample. Richardson plot shows linear variation indicating ideal heterojunction case. To study the nature of the injection of charge carriers from the metal electrode to film samples, electrode limited conduction mechanisms are analyzed using the Schottky emission model. Overall observations show enhancement in electrical characteristics in MFO-PVA nanocomposite film than that of pristine PVA film. In this study, MFO-PVA nanocomposite film demonstrates potential for applications in different domains due to its versatile properties.

Acknowledgements

This work is financially supported by DST-SERB (Grant No. EMR/2016/001409), Govt. of India. One of the authors (MH) would like to acknowledge DST-INSPIRE for providing fellowship.

Author contribution

MH: Investigation, Formal analysis, Writing original draft, Validation; SA: Investigation, Formal analysis, Validation; RS: Resources, Validation; AKM: Supervision, Conceptualization, Methodology, Visualization, Validation, Project administration.

Data availability statement

Data will be made available on reasonable request.

Declarations

Conflict of interest There are no conflicts to declare.

References

1. I. Saini, A. Sharma, R. Dhiman, S. Aggarwal, S. Ram, P.K. Sharma, *J. Alloys Compd.* **714**, 172 (2017)
2. A.K. Das, S. Sinha, A. Mukherjee, A.K. Meikap, *Mater. Chem. Phys.* **167**, 286 (2015)
3. S.H. Hosseini, A. Asadnia, *Int. J. Phys. Sci.* **8**, 1209 (2013)
4. A. Han, J. Liao, M. Ye, Y. Li, X. Peng, *Chin. J. Chem. Eng.* **19**, 1047 (2011)
5. A. Hasan, A.M.E. Sayed, W.M. Morsi, S.E. Sayed, *J. Appl. Phys.* **112**, 093525 (2012)
6. J. Huang, Y. Cao, X. Zhang, Y. Li, J. Guo, S. Wei, X. Peng, T.D. Shen, Z. Guo, *AIP Adv.* **5**, 097813 (2015)
7. S. Shafiu, R. Topkaya, A. Baykal, M.S. Toprak, *Mater. Res. Bull.* **48**, 4066 (2012)
8. M. Rezaei, S.M. Mirkazemi, S. Alamolhoda, *J. Supercond. Nov. Magn.* **34**, 1397 (2021)
9. G. Nasar, M. Ishfaq, F. Ahmad, S. Nazir, F. ur Raheem, *J. Mater. Phys. Sci.* **1**, 87 (2020)
10. H.M. Alhusaiki-Alghamdi, *J. Nanoelectron. Optoelectron.* **17**, 147 (2022)
11. B. Salah, A.I. Ayesh, *Molecules* **26**, 121 (2021)
12. R. Sahanakumari, V. Ravindrachary, B.K. Mahantesha, R. Padmakumari, P. Tegginamata, *J. Phys.: Conf. Ser.* **1172**, 012077 (2019)
13. M. Halder, A. Tiwari, A.K. Meikap, *AIP Conf. Proc.* **2265**, 030442 (2020)
14. K.K. Srivastava, A. Kumar, O.S. Panwar, K.N. Lakshminarayan, *J. Non-Crys. Solids* **33**, 205 (1979)
15. A.K. Zak, W.H.A. Majid, M.E. Abrishami, R. Yousefi, *Solid State Sci.* **13**, 251 (2011)
16. P. Bindu, S.J. Thomas, *Theo. Appl. Phys.* **8**, 123 (2014)
17. H. Schmid, *Ferroelectrics* **162**, 317 (1994)
18. R. Ertugrul, A. Tataroghi, *Chinese Phys. Lett.* **29**, 5 (2012)
19. R. Sinha, S. Basu, A.K. Meikap, *Physica E* **69**, 47 (2015)
20. P.H. Bell, W.P. Davey, *J. Chem. Phys.* **9**, 441 (1941)
21. K. Kumari, A. Prasad, K. Prasad, *Am. J. Mater. Sci.* **6**, 1 (2016)
22. S.K. Patri, P.L. Deepti, R.N.P. Choudhary, B. Behera, *J. Electroceram.* **40**, 338 (2018)
23. M. Halder, A.K. Das, A.K. Meikap, *Mater. Res. Bull.* **104**, 179 (2018)

24. M. Sharma, S.K. Tripathi, *Optoelectro. Adv. Mater.: Rapid Commun.* **6**, 200 (2012)
25. K. Jung, Y. Kim, H. Im, *J. Korean Phys. Soc.* **59**, 2778 (2011)
26. A.K. Das, R. Dharmana, A. Mukherjee, K. Baba, R. Hatada, A.K. Meikap, *J. Appl. Phys.* **123**, 145105 (2018)

Publisher's Note Springer Nature remains neutral with regard to jurisdictional claims in published maps and institutional affiliations.

Springer Nature or its licensor holds exclusive rights to this article under a publishing agreement with the author(s) or other rightsholder(s); author self-archiving of the accepted manuscript version of this article is solely governed by the terms of such publishing agreement and applicable law.